



Lee waves detection over the Mediterranean Sea using the Advanced Infra-Red Water Vapour Estimator (AIRWAVE) Total Column Water Vapor (TCWV) dataset

Enzo Papandrea^{1,2}, Stefano Casadio^{1,3}, Elisa Castelli², Bianca Maria Dinelli², and Mario Marcello Miglietta²

¹Serco Italia s.p.a., via Sciadonna 24-26, 00044 Frascati, Italy

²Istituto di Scienze dell'Atmosfera e del Clima, ISAC-CNR, Via Gobetti 101, 40129 Bologna, Italy

³European Space Agency (ESA/ESRIN), Via Galileo Galilei 1, 00044 Frascati, Italy

Correspondence: Enzo Papandrea (Enzo.Papandrea@serco.com)

Abstract. Atmospheric gravity waves generated downstream by the orography in a stratified airflow are known as lee waves. In the present study, such mesoscale patterns have been detected, over water and in clear sky conditions, using the Advanced Infra-Red Water Vapour Estimator (AIRWAVE) Total Column Water Vapour (TCWV) dataset, which contains about 20-year day-night products, obtained from the thermal infra-red measurements of the Along Track Scanning Radiometer (ATSR) instrument series. The good accuracy of such data, along with the native $1 \times 1 \text{ km}^2$ spatial resolution, allows the investigation of small scale features as the lee waves. In this work, we focused on the Mediterranean region, the largest semi-enclosed basin on the Earth. The peculiarities of this area, which is characterized by complex orography and rough coastlines, lead indeed to a possible development of these structures both over land and over sea. We developed an automatic tool for the rapid detection of areas with high probability of lee waves occurrence, exploiting the TCWV variability in spatial regions $0.15^\circ \times 0.15^\circ$ wide. Through this analysis, several occurrences of structures connected with lee waves have been observed. The waves are detected in spring, fall and summer seasons, with TCWV values usually falling in the range from 15 to 35 kg m^{-2} . In this article we describe some cases over the Central (Italy) and the Eastern Mediterranean basin (Greece, Turkey, Cyprus). We compared a case of perturbed AIRWAVE TCWV fields due to lee waves occurred over the Tyrrhenian Sea on 18 July 1997 with the sea surface winds from the Synthetic Aperture Radar (SAR), which sounded the same geographical area, finding a good agreement. Another case has been investigated in detail: on 2 August 2002 the Aegean sea region was almost simultaneously sounded by both ATSR-2 and AATSR instruments. The AIRWAVE TCWV fields derived from the two sensors were successfully compared with the vertically integrated water vapour content simulated with the Weather Research and Forecasting (WRF) numerical model for the same time period, confirming our findings. Wave parameters such as amplitude, wavelength and phase, are described through the use of the “Morlet” Continuous Wavelet Transformation (CWT). The performed analysis derived typical wavelengths from 6 to 8 km and amplitude that may extend up to 20 kg m^{-2} .



1 Introduction

Atmospheric gravity waves (AGW) may be generated in a stably stratified atmosphere when an airflow impinges on orographic obstacles, like isolated mountains or islands. AGW may develop in both upstream and downstream directions. However, in situations where the wave energy is ducted close to the surface, the motion is confined downstream in the lower atmosphere and the waves are located within a wedge-shaped wake behind the obstacle (Vosper et al., 2006). Most of the observed AGW fall in the latter group and they are referred to as trapped “lee waves” (Li et al., 2011). The waves may be classified into two different categories: a) diverging wave type, characterised by crests orientated outwards from the centre of the wake; b) transverse wave type, where the crests are nearly perpendicular to the wind direction (Gjevik and Marthinsen, 1978). Lee waves may play an important role in modifying the vertical structure of wind, moisture, and temperature near and behind an obstacle, being nowadays a well-recognized cause of hazard to aviation, especially under dry conditions, when they do not generate clouds and, thus, cannot be easily detected. (Christie, 1983; Uhlenbrock et al., 2007). In specific circumstances (e.g. as a consequence of the interaction with extensive mountain ranges), non-linear perturbations may also interact with larger-scale flow, impacting on the global scale circulation and the climatological momentum balance (Wurtele et al., 1993). Therefore, the study of such phenomena is of broad relevance. Lee waves can be identified through the use of satellite instruments, e.g. the Synthetic Aperture Radar (SAR), that can detect, in the backscattered radar power, the small-scale sea surface roughness, enabling to estimate the varying wind speeds at the sea surface (Cheng and Alpers, 2010).

Background concentrations of atmospheric constituents, such as the Total Column of Water Vapour (TCWV), are also perturbed by AGW. Therefore, TCWV fields, derived e.g. from satellite instruments, can also be used for lee waves identification. The only constraint is that their accuracy and resolution have to be sufficiently high. Water vapour is a highly variable gas, its concentration can span several orders of magnitude in the lower atmosphere. It has a major role in transporting latent heat and, for this reason, is a principal element in the thermodynamics of the atmosphere (Jacob, 2001). It is the most important natural greenhouse gas in the Earth’s atmosphere, accounting for about half of the present-day greenhouse effect, and it is the dominant gaseous source of infra-red opacity in the atmosphere (Held and Soden, 2000). Accurate knowledge of atmospheric water vapour is therefore important and a big effort is made by Space Agencies and by the Scientific Community to globally derive its abundance using a wide range of techniques and observational platforms. The columnar water vapour fields obtained from the Moderate Resolution Imaging Spectroradiometer (MODIS) (Salomonson et al., 2002) has already been used to observe mountain lee waves over land: water vapour is derived from the $6.7 \mu\text{m}$ channel whose peak sensitivity is at 550 hPa (about 5 km) in the free troposphere (Uhlenbrock et al., 2007). More recently, mountain lee waves have also been identified in the MODIS TCWV product derived from Near-Infrared (NIR) $0.94 \mu\text{m}$ measurements, which are sensitive to atmospheric features very close to the surface (Lyapustin et al., 2014). The perturbations of the vertical structure of the planetary boundary layer, causing quasi-periodic oscillations of columnar water vapour, aerosol optical depth, and surface irradiance in different spectral bands have also been detected using ground-based observations collected at Lampedusa, in the central Mediterranean Sea (Di Sarra et al., 2013). The authors were also able to estimate the Saharan dust radiative forcing variations during the gravity wave event.



Miglietta et al. (2010) showed that the simulations performed with the Weather Research and Forecasting (WRF) model are able to reproduce the near-surface wind speed variability due to gravity waves. Model lee wave features are similar to the sea surface wind patterns extracted from the ENVironmental SATellite (ENVISAT) Advanced Synthetic Aperture Radar (ASAR) images, proving that the model is able to represent such phenomena in a realistic way.

5 Recently, (Casadio et al., 2016) have developed the Advanced Infra-Red WAter Vapour Estimator (AIRWAVE) algorithm to obtain the TCWV from the measurements of the Along Track Scanning Radiometer (ATSR) instrument series. The application of the AIRWAVE algorithm (Casadio et al., 2016) to the measurements of the ATSR missions (Delderfield et al., 1986) has produced a dataset of about 20 years of day-night TCWV, retrieved over water in clear sky conditions, at the native $1 \times 1 \text{ km}^2$ spatial resolution grid. The dataset has been recently used to detect trends in the Inter Tropical Convergence Zone (ITCZ)
10 latitudinal displacement over the full ATSR missions (Castelli et al., 2018a). The overall good quality of the AIRWAVE products has been verified using both satellite and radiosonde correlative measurements (Papandrea et al., 2018; Schröder et al., 2018). To date, the dataset is available in two versions; the latest version (V2) is obtained with an improved version of the AIRWAVE algorithm which accounts for the atmospheric variability at different latitudes and associated seasonality, reducing both biases and root square mean error, especially in polar and coastal regions (Castelli et al., 2019). The overall good quality
15 of the dataset suggested that it could be used for systematic lee waves detection. Indeed, oscillations of the TCWV in regions where lee waves can form have been found during quality checks of the AIRWAVE dataset (Castelli et al., 2018b).

In this article we describe a method developed for the detection of wave structures in the AIRWAVE dataset, focusing on the Mediterranean region. The detections are obtained through an automatic tool that exploits the TCWV variability in spatial regions of appropriate extension. A subset of the identified occurrences is compared both with correlative measurements from
20 the SAR instrument onboard the European Remote Sensing (ERS)-2 satellite and with WRF model simulations, strengthening the reliability of the lee waves identification in the AIRWAVE dataset.

The paper is organized as follows: in section 2 we describe the approach followed for the automatic lee waves detection and we show some selected occurrences; in section 3 we describe a case occurred on 18 July 1997, comparing the AIRWAVE TCWV values with the SAR/ERS-2 fields, and a case detected on 2 August 2002 (when both ATSR-2 and AATSR sounded
25 the Aegean sea region at very close times), comparing the AIRWAVE TCWV fields with WRF simulations; in section 4 we perform a wave characterization using the Continuous Wavelet Transformation (CWT) and, finally, conclusions are given in section 5.

2 Lee waves detection using the AIRWAVE dataset

The quality of the AIRWAVEv2 TCWV dataset (Castelli et al., 2019) was verified not only using external correlative measure-
30 ments but also adopting internal quality checks (e.g. range of validity of the TCWV values and their spatial variability). The analysis highlighted the overall good quality of the dataset but also showed a recurrent higher variability in specific areas in the Mediterranean region. We noticed that all these occurrences were associated with lee wave patterns, generated by airflows crossing one or more obstacles (Castelli et al., 2018b). These phenomena indeed induce water vapour perturbations very close



to the surface, yielding the TCWV amounts very sensitive to them. Considering the small scale of these patterns, the native $1 \times 1 \text{ km}^2$ spatial resolution of the AIRWAVE dataset is suitable to capture the TCWV variations associated with lee waves.

Given that AIRWAVE TCWV could detect lee waves, we designed a systematic approach for the statistical analysis of these events. The very large number of ATSR products, covering about 20 years of measurements, requires an automatic and efficient tool for a systematic detection of the waves. The basic idea for the development of this tool is that the presence of waves produces a local enhancement in the TCWV variability. To detect this variability enhancement, we divided the examined region into regular grid cells of dimensions fine enough to capture the geographic details of the studied areas but large enough to contain an appropriate number of measurements in order to highlight the variability. For each grid cell, we computed the standard deviation (STD) of the observed TCWV. Background STD was estimated as the standard deviation of the monthly mean computed in grid cells in Mediterranean areas where lee waves occurrence was unlikely. We then evaluated the Normalised Standard Deviation (NSTD) as the STD found in the examined areas divided by the background STD. The normalization was performed in order to minimise the dependence of the results on intrinsic atmospheric variability and instrument characteristics (e.g. measurements noise) and allows to use the same classification criteria for all the instruments in the ATSR series (ATSR-1, ATSR-2 and AATSR) and for all the seasons.

The size of the grid cells is a critical issue in our method: different grid sizes have been tested and a regular latitude-longitude grid, with each grid cell covering an area of $0.15^\circ \times 0.15^\circ$ (about $17 \times 13\text{-}14 \text{ km}^2$ at $35/40$ latitude degrees) was found to give the best performance. Each cell is included in our analysis only if the amount of cloud free TCWV products is larger than 20 %, in order to ensure robust statistics. At latitudes typical of the investigated areas, this choice allows, within each grid cell, to consider a number of TCWV products which enables to reduce, in the pixel aggregation process, the noise to less than 1 % (the single pixel noise error was estimated to be 4.8 % / 5.2 % for AATSR / ATSR-2 at mid-latitude, for more details see Castelli et al. (2019)).

The scenes have been classified with the adoption of two criteria, both applied on the latitude-longitude regular grid. The first one is based on the percentage of cloud-free scenes (we label the associated threshold as TR1) and the second one on the percentage of grid cells having NSTD values exceeding the value of 2 (labeled as TR2). The aim of this selection scheme is to detect the most evident cases of lee waves in scenes characterized by a sufficient number of available (i.e. cloud-free) measurements. The classification of the most representative events was populated with the scenes where both the criteria TR1 > 70 % and TR2 > 1 % were satisfied. We mainly considered, for the lee waves detection, three Mediterranean sub-basins, which are shown in the top-left map of Fig. 1. The first two are located over the central Mediterranean Sea and include mainly the Tyrrhenian Sea (R1) and the Southern Tyrrhenian Sea / Ionian Sea (R2), while the other is located on the Eastern Mediterranean Sea (R3). In the whole AIRWAVE dataset, we found about thirty occurrences in R1+R2 and fifty in R3. The relatively low number of detections is related to the revisit time over one specific location (about 3 days) due to the limited ATSR across track swath (about 500 km wide).

Figure 1 shows the total number of monthly TCWV waves occurrences as a function of the month of the year (black curve). About 76 % of the selected cases are detected in JJA (June-July-August), 17 % in MAM (March-April-May) and the remaining 7 % scenes in SON (September-October-November). Since we use only “cloud-free” measurements to detect the



TCWV waves occurrences, the number of identified cases depends upon the amount of available cloud-free data. In order to estimate the typical number of cloud-free pixels in each month, we performed an analysis using all the available AATSR measurements for the whole year 2003. In Fig. 1 the monthly means of the percentage of cloud-free measurements are also plotted, using different colours according to the different geographical regions shown on the map. The highest number of available observations is expected during August, in particular over the Eastern Mediterranean Sea (about 80 %), while the lowest observations amount is found in the DJF (December-January-February) season (about 20 %), thus they correspond pretty well with the number of wave detections.

The Aegean Sea is particularly suitable for the observation of these phenomena. From Spring to Fall, the Northern Aegean is often crossed by north-easterly winds, called Etesians (Kotroni et al., 2001; Miglietta et al., 2017), that change direction (becoming north-westerly or westerly) and intensify over the Southern Aegean, approaching JJA monthly averages of about 8-10 m s⁻¹ in part of the Cyclades, of the Dodecanese Islands and East of Crete (e.g. Vagenas et al., 2017). Often, anticyclonic circulations, typical of summertime in the region, determine clear sky conditions. The complexity of the coastal orography and the presence of mountainous islands deeply influence the local-scale atmospheric circulation in the Ekman layer, producing local effects at spatial scales down to a few kilometres (Vagenas et al., 2017).

As an example of detection, Fig. 2 shows the AATSR TCWV fields (left panel) and the corresponding NSTD over the Aegean Sea (right panel) for 2 August 2002. In this figure, the wind speeds and directions, obtained from ERA-Interim products at grid resolution 1.0° × 1.0°, are indicated with white arrows. The reported speeds have been derived using a linear interpolation over time of the 10 m (u and v) wind components, available every six hours. The left panel of Fig. 2 clearly shows the lee wave structure of the AATSR TCWV, while the right panel of the same figure, showing the NSTD, clearly demonstrated the correct geolocation of the lee wave area of our tool. In correspondence with the TCWV waves, the NSTD value increases with respect to the background values, being the patterns clearly correlated with the wind direction. Areas characterized by shorter wavelengths or/and by wider wave amplitudes generate larger standard deviations.

Several lee wave occurrences have been found close to the island of Crete, which has an elongated shape, spanning 260 km from East to West, while its North-South extension ranges from 12 to 60 km. The shape of the island and the presence of elevated mountain regions (up to 2450 m a.s.l.) directly reflect in wave-like patterns. Other occurrences have been found close to Sardinia and Corsica and near Cyprus.

Figure 3 shows the NSTD observed for a set of selected lee waves events. Two cases are located between Sardinia, Corsica and the Italian Peninsula, over the Tyrrhenian Sea (panels g and h). One event is located in the Eastern Mediterranean across the island of Cyprus (panels f) and the remaining five over the Aegean Sea (panels a-e). In the figure, two cases are measured at two different times of the same day: panels a) and b) are obtained from, respectively, ERS-2 morning and evening satellite passes for the same day with local crossing time at approximately 10:20 (descending) and 22:20 (ascending).

The ECMWF wind speeds for the selected events are shown with white arrows superimposed to the mapped NSTD. The figure indicates that the patterns of the normalised standard deviation are evidently correlated with the wind direction. The atmospheric conditions of the reported cases, all characterized by intense and constant winds direction, allowed the AGW propagation over long horizontal distances, trapping the wave vertically. Wind jets and wakes in the lee of mountain ranges



may indeed generate horizontal wind shear which may propagate in a wave duct or wave guide horizontally over distances even of several hundreds of kilometres (Cheng and Alpers, 2010).

3 Validation of the Lee waves detections

In order to find scientific evidence that the detected structures are indeed lee waves, we selected a subset of lee wave occurrences and we compared them with both independent observations and model simulations. We found one particular case where the lee waves were measured almost simultaneously by two ATSR instruments. The comparison of the results of the detection algorithm applied to the two instruments enabled the assessment of its robustness, since each instrument has its own characteristics (e.g. noise, systematic errors), which may act in a different way on their measurements. This lee wave detection was then compared to the outputs of a state-of-the-art numerical limited area model, using the outputs of a WRF model run (see Sect. 3.1).

We also searched for possible inter-comparison of the AIRWAVE TCWV fields with the SAR sea surface winds, using the available space/time coincidences. We found one particular case, which is suitable for our purpose adopting, as correlative variable, wind fields from the ERS-2 SAR image products (see Sect. 3.2).

In all the aforementioned comparison exercises, we observed the presence of similar structures both in the AIRWAVE dataset and in the correlative data, thus enhancing the level of confidence of the detected AIRWAVE lee waves events (see Sect. 3.1). The performed comparisons are illustrated in more details in the following subsections.

3.1 ATSR-2 and AATSR almost simultaneous measurements and WRF model comparison

On 2 August 2002 the Aegean Sea area was sounded by both ATSR-2 (onboard ERS-2 satellite) and AATSR (on board ENVISAT) that were almost simultaneously (with a 30 minutes delay over the same orbital path) flying above the region. This “tandem” configuration offers an important possibility to compare the TCWV products of the two sensors, which are similar in design but are characterised by different random and systematic error components.

North-westerly winds were blowing with high intensity. Furthermore, the cloud masks of the two sensors indicate that the sky over the sea was almost entirely cloud-free. The ATSR-2 instrument covered, about half an hour later than AATSR, the same region. Our algorithm detected lee waves in the TCWV fields derived from the measurements of the two sensors, both showing a similar pattern. In particular, the lee waves were located in the South-East of Central Greece (Evia Island) and of numerous Cyclades and Dodecanese Islands (Andros, Tinos, Amorgos, Ikaria, Samos, Kos, and, toward the South, up to Crete, Karpathos and Kassos), as can be seen in the TCWV fields and in the corresponding NSTD map shown in Fig. 2.

We investigated in more detail the geographical area surrounded by the red box in Fig. 2. Figure 4 reports the AIRWAVE TCWV values of this region, for both ATSR-2 and AATSR, in the left and right panels respectively. In this region, the Amorgos island has an important role in the development of the lee waves. Amorgos is a long and narrow island, with a length of 32 km and a width ranging between 1.9 and 5.5 km. It has relatively high mountains (three of them over 500 m a.s.l.) that fall steeply into the sea. The wind direction on 2 August 2002 was almost perpendicular to the island main axis, as indicated by



the ECMWF ERA-Interim wind speeds and directions, which are superimposed in the figure. All these conditions led to the formation of observed trapped waves, that extended several kilometres away from the source, clearly visible in the figure as alternate darker and lighter stripes. In Fig. 4 a very large correlation between the two AIRWAVE datasets can be noticed. This suggests that the observed pattern is real and not an artefact of the measurements.

5 To strengthen the robustness of our analysis, we have used the WRF model to simulate the atmospheric conditions of the sounded area. The Advanced Research WRF model (WRF-ARW version 3.5.1; Wang et al. (2010)) was here implemented with a grid spacing sufficiently fine for the simulation of small-scale atmospheric waves. In this work, it was implemented in a one-way nested 3-grid configuration, with 40 vertical levels and horizontal grid spacing respectively of 16, 4, and 1 km. 400×400 grid points are used in the inner domain, covering the area ($33.6^\circ \text{N} - 37.4^\circ \text{N}$, $24.7^\circ \text{E} - 29.2^\circ \text{E}$). ECMWF analysis/forecasts
10 are used as initial/3-hourly boundary conditions. The model simulation starts at 00:00 UTC, 2 August 2002, and lasts for 24 hours, so that the times of satellite observations are definitely after the model spin-up time. The following parameterization schemes are employed: the Thompson et al. (2008) microphysics; the Rapid Radiative Transfer Model (RRTM) for longwave radiation (Mlawer et al., 1997); the Dudhia (1989) scheme for shortwave radiation; the unified Noah land-surface model (Niu et al., 2011); Mellor–Yamada–Janjić for the planetary boundary layer (Janjić, 2001). In the past, the model was successfully
15 employed, with a similar configuration, to simulate wind speed in two case studies of orographic lee waves over the Eastern Mediterranean Sea in comparison with SAR retrieval (Miglietta et al., 2013).

In Fig. 4, the modeled vertically integrated water vapour values are superimposed to the ATSR TCWV fields (for the sake of image readability, only two contour levels are shown). The model foresees the presence of waves, with similar periodicity and direction as the ones detected by AIRWAVE, capturing very well the South-Eastward lee waves extending from the Cyclades
20 islands of Amorgos and Anafi. The presence of a wave-like pattern variability of the lower troposphere was also confirmed from the WRF geopotential and temperature fields (not shown).

3.2 ATSR-2 and SAR comparison

An opportunity for comparison with independent correlative data was found for the event occurred on 18 July 1997. During that day, the Tyrrhenian Sea region was sounded by both the ATSR-2 instrument and the SAR instrument onboard the same
25 ERS-2 satellite. Strong westerly winds blew across the island of Sardinia and in the Tyrrhenian Sea, with direction and strength almost constant in the considered basin.

An enhancement of the NSTD, derived from the ATSR-2 AIRWAVE TCWV fields of the ERS-2 orbit 11734, was detected in many grid cells of the considered region, as shown in the top panel of Fig. 5. The corresponding TCWV values, shown in the central panel of the figure, highlight that the winds crossing the Sardinia island, which are obtained from the ERA-Interim fields
30 at $1.0^\circ \times 1.0^\circ$, clearly imprint wave patterns over the sea induced by the orography of the island. The formed lee waves propagate downstream for hundreds of kilometres in the Tyrrhenian Sea towards the Italian peninsula. The observed TCWV fluctuations can be compared to the SAR wind fields, shown in the single look complex images for the same day reported in the bottom panel of Fig. 5. The picture has been obtained using the Earth Observation Link (EOLi, <https://earth.esa.int/web/guest/eoli>) European Space Agency's client for Earth Observation Catalogue Service. The EOLi tool allows the selection of Earth Observation



products acquired by the ERS and ENVISAT satellites and the display of the related images on the top of an orthographic representation of the Earth.

The spatial resolution of the SAR/ERS-2 images is very high: 26 m in range (across track) and between 6 and 30 m in azimuth (along track). The swath width of the sensor is about 100 km, thus covering only a portion of the AIRWAVE products in the longitude domain. The lee wave patterns shown in the SAR images downstream of the island of Sardinia reflect the sea surface fingerprints of the perturbations in the lower troposphere. The patterns are in agreement with those derived from the AIRWAVE dataset. In particular, the geographical regions where the trapped lee waves are located in both figure panels, which are delimited by the red bounding box in order to facilitate the reader identification, are consistent between the two sensors.

4 Lee waves characterization

As described in Section 2, the first step of our methodology consists in the detection of the lee waves occurrences. Once the lee waves are found, it will be desirable to have a tool that can provide quantitative information about the wave “local” characteristics, such as amplitudes and wavelengths estimated in different locations of the considered areas. For this purpose, we tested the wavelet approach proposed by Torrence and Compo (1998), which was found suitable to characterize local non-stationary signals. The method used here is based on the “Morlet” Continuous Wavelet Transformation (CWT), a tool that can be used to analyze scale-dependent structures of a signal as it varies in time (or in space) (Sadowsky, 1996). Several practical aspects of the analysis are reported in Torrence and Compo (1998), using time series of the El Niño–Southern Oscillation (ENSO) as a possible example of its application. The CWT approach has been successfully applied to several studies, e.g. to mesoscale gravity waves (Lu et al., 2005; Koch et al., 2005) or for the characterization and removal of non-stationary and localized vertical structures in atmospheric temperature and density profiles retrieved from satellites (Iannone et al., 2014).

In this work, we used the wavelet software packages, developed by Torrence and Compo (1998) in a series of different programming languages and available at (<http://paos.colorado.edu/research/wavelets/>). We applied the CWT method to the AIRWAVE TCWV fields shown in Fig. 4. The analysis was performed in the along track direction (i.e. coincident with the satellite motion) because, in the selected cases, it was almost aligned with the wind fields and therefore with the wave pattern. The method computes the energy of spectral components as a function of along track position (associated with a value of latitude, longitude and TCWV amount) and of the oscillation wavelength. For each along track position, we then selected the wavelength corresponding to the most energetic wave. Repeating the analysis for each vector corresponding to a different across track position, we finally obtained the output of the analysis reported in Fig. 6. In the figure, the left panel shows the analysis for the ATSR-2 orbit number 38086, while the right panel for the AATSR orbit number 2214.

We considered only wave power values within the “95 % confidence interval” which is obtained comparing the spectrum of individual wavelength series against a certain background level (the red noise) (Torrence and Compo, 1998). Furthermore, we selected only wavelength values within the space/frequency region determined using the so-called Cone Of Influence (COI), which is the region where the wavelet power spectra values can be considered unbiased by edge effects. The analysis shows that the majority of the TCWV fluctuations are statistically significant, both for AATSR and for ATSR-2. Wavelengths



were detected mainly from 6 to 8 km (associated with azure-green colours in Fig. 6) with amplitudes up to 75 % of the average TCWV amounts. Our findings are confirmed by the theoretical study performed by Nappo (2013). The paper states that the most energetic wavenumber k_{max} can be easily predicted using a mechanical approximation for lee wave calculations, assuming a spectrum of horizontal wavenumbers with $k_{max} = 4b$, where b is the scale width of the mountain, computed as the distance between the maximum height and the point where the altitude reaches half of the maximum. Since the island of Amorgos is characterized by scale widths ranging from 1.0 to 2.0 km, this leads to a prediction of wavelengths ranging from 4 to 8 km, consistent with the wavelet analysis.

5 Conclusions

We have identified, over the Mediterranean basin, several lee waves occurrences. The scenes have been detected using the AIRWAVE total column water vapour dataset, containing about 20-year day-night products over water in clear-sky conditions and derived from the ATSR instrument series. The high ($1 \times 1 \text{ km}^2$) spatial resolution of the adopted database is an essential requisite for the detection of these phenomena. We have investigated the regions over the Tyrrhenian and Aegean seas, finding that the Greece basin is the place where lee waves are observed with the highest frequency, due to its complex orography and coastlines and to the presence of intense winds and clear sky conditions during most of the year. The selection has been performed with an automatic tool that computes the TCWV standard deviation in spatial regions about 200/250 km^2 wide and classifies the cases based on the number of clear-sky measurements and according to the derived normalised standard deviation. We verified that the adopted method do not produce “false positive” detections in regions where the presence of lee wave events is not expected (e.g. open ocean). We carried out a validation on a subset of lee wave occurrences, finding the presence of similar structures both in the AIRWAVE dataset and in the correlative data (independent observations or WRF model simulations). Through the Morlet continuous wavelet transformation analysis, we were able to determine the characteristics of the observed lee waves in a region located South-West of the narrow island of Amorgos, calculating wavelength values ranging from 6 to 8 km with amplitudes up to 75 % of the average TCWV amounts for a typical case study. The values are reasonable from a theoretical point of view and were confirmed by a WRF model run performed for the selected case. Therefore, the wavelength analysis adopted in this work has been found appropriate. Nevertheless, we are investigating the possibility to develop a more sophisticated method for a statistical analysis of these events.

The proposed approach, as it does not rely on external information, could in principle be applied to high spatial resolution TCWV products from other satellite instruments. The method is also very efficient from a computational point of view and is therefore suitable for near real-time detection of lee waves from current flying sensors measurements, e.g. the Sea and Land Surface Temperature Radiometer (SLSTR), onboard Copernicus Sentinel-3 (Donlon et al., 2012). The tool can also be applied to other regions of the Earth. Future developments include a possible evaluation of radiative forcing variations associated to wave events and a more accurate characterization of the waves exploiting the “tandem periods” when measurements of two instruments almost overlap (e.g. SLSTR/Sentinel-3a and SLSTR/Sentinel-3b).



Author contributions. EP, EC, SC, BMD conceived the method. MMM performed the WRF model simulations. EP performed the validation, the wavelet analysis and drafted the paper. All authors discussed the results, read and commented on the manuscript.

Competing interests. The authors declare that they have no conflict of interest.

Acknowledgements. This work has been performed under the ESA/ESRIN IDEAS+ contract no. 4000108531/13/I-NB. MMM gratefully
5 acknowledges the funding from the European Commission (Project “CEASELESS”, grant agreement no. 730030).



References

- Casadio, S., Castelli, E., Papandrea, E., Dinelli, B. M., Pisacane, G., Burini, A., and Bojkov, B. R.: Total column water vapour from along track scanning radiometer series using thermal infrared dual view ocean cloud free measurements: The Advanced Infra-Red Water Vapour Estimator (AIRWAVE) algorithm, *Remote sensing of environment*, 172, 1–14, <https://doi.org/10.1016/j.rse.2015.10.037>, 2016.
- 5 Castelli, E., Papandrea, E., Valeri, M., Greco, F. P., Ventrucci, M., Casadio, S., and Dinelli, B. M.: ITCZ trend analysis via Geodesic P-spline smoothing of the AIRWAVE TCWV and cloud frequency datasets, *Atmospheric Research*, 214, 228–238, <https://doi.org/10.1016/j.atmosres.2018.07.019>, 2018a.
- Castelli, E., Miglietta, M. M., Dinelli, B. M., Stefano, C., Papandrea, E., and Bojkov, B.: Atmospheric Lee waves over the Eastern Mediterranean Basin as seen by the AIRWAVE Total Column Water Vapor and the WRF model, in: EUMETSAT Meteorological Satellite Conference 2018, Tallin, Estonia, 17-21 September 2018, 6.3_192, 2018b.
- 10 Castelli, E., Papandrea, E., Di Roma, A., Dinelli, B. M., Casadio, S., and Bojkov, B.: The Advanced Infra-Red Water Vapour Estimator (AIRWAVE) version 2: algorithm evolution, dataset description and performance improvements, *Atmospheric Measurement Techniques*, 12, 371–388, <https://doi.org/10.5194/amt-12-371-2019>, 2019.
- Cheng, C. M. and Alpers, W.: Investigation of trapped atmospheric gravity waves over the South China Sea using Envisat synthetic aperture radar images, *International Journal of Remote Sensing*, 31, 4725–4742, <https://doi.org/10.1080/01431161.2010.485145>, 2010.
- 15 Christie, D. R.: Solitary waves as aviation hazard, *Eos, Transactions American Geophysical Union*, 64, 67–67, <https://doi.org/10.1029/EO064i007p00067-01>, 1983.
- Delderfield, J., Llewellyn-Jones, D. T., Bernard, R., De Javel, Y., Williamson, E. J., Mason, I., Pick, D. R., and Barton, I. J.: The along track scanning radiometer (ATSR) for ERS1, in: *Instrumentation for optical remote sensing from space*, vol. 589, pp. 114–121, International Society for Optics and Photonics, 1986.
- 20 Di Sarra, A., Fuà, D., and Meloni, D.: Estimate of surface direct radiative forcing of desert dust from atmospheric modulation of the aerosol optical depth, *Atmospheric Chemistry and Physics*, 13, 5647–5654, <https://doi.org/10.5194/acp-13-5647-2013>, 2013.
- Donlon, C., Berruti, B., Buongiorno, A., Ferreira, M.-H., Féménias, P., Frerick, J., Goryl, P., Klein, U., Laur, H., Mavrocordatos, C., Nieke, J., Rebhan, H., Seitz, B., Stroede, J., and Sciarra, R.: The global monitoring for environment and security (GMES) sentinel-3 mission, *Remote Sensing of Environment*, 120, 37–57, <http://dx.doi.org/10.1016/j.rse.2011.07.024>, 2012.
- 25 Dudhia, J.: Numerical study of convection observed during the winter monsoon experiment using a mesoscale two-dimensional model, *Journal of the atmospheric sciences*, 46, 3077–3107, [https://doi.org/10.1175/1520-0469\(1989\)046<3077:NSOCOD>2.0.CO;2](https://doi.org/10.1175/1520-0469(1989)046<3077:NSOCOD>2.0.CO;2), 1989.
- Gjevik, B. and Marthinsen, T.: Three-dimensional lee-wave pattern, *Quarterly Journal of the Royal Meteorological Society*, 104, 947–957, <https://doi.org/10.1002/qj.49710444207>, 1978.
- 30 Held, I. M. and Soden, B. J.: Water vapor feedback and global warming, *Annual review of energy and the environment*, 25, 441–475, <https://doi.org/10.1146/annurev.energy.25.1.441>, 2000.
- Iannone, R. Q., Casadio, S., and Bojkov, B.: A new method for the validation of the GOMOS high resolution temperature profiles products, *Annals of Geophysics*, 57, 0546, <https://doi.org/10.4401/ag-6487>, 2014.
- Jacob, D.: The role of water vapour in the atmosphere. A short overview from a climate modeller's point of view, *Physics and Chemistry of the Earth, Part A: Solid Earth and Geodesy*, 26, 523–527, [https://doi.org/10.1016/S1464-1895\(01\)00094-1](https://doi.org/10.1016/S1464-1895(01)00094-1), 2001.
- Janjić, Z. I.: Nonsingular implementation of the Mellor-Yamada level 2.5 scheme in the NCEP Meso model, NCEP Tech. Rep., 437, 61 pp., http://www2.mmm.ucar.edu/wrf/users/phys_refs/SURFACE_LAYER/eta_part4.pdf, 2001.



- Koch, S. E., Jamison, B. D., Lu, C., Smith, T. L., Tollerud, E. I., Girz, C., Wang, N., Lane, T. P., Shapiro, M. A., Parrish, D. D., and Cooper, O. R.: Turbulence and gravity waves within an upper-level front, *Journal of the atmospheric sciences*, 62, 3885–3908, <https://doi.org/10.1175/JAS3574.1>, 2005.
- Kotroni, V., Lagouvardos, K., and Lalas, D.: The effect of the island of Crete on the Etesian winds over the Aegean Sea, *Quarterly Journal of the Royal Meteorological Society*, 127, 1917–1937, <https://doi.org/10.1002/qj.49712757604>, 2001.
- Li, X., Zheng, W., Yang, X., Li, Z., and Pichel, W. G.: Sea surface imprints of coastal mountain lee waves imaged by synthetic aperture radar, *Journal of Geophysical Research: Oceans*, 116, <https://doi.org/10.1029/2010JC006643>, 2011.
- Lu, C., Koch, S. E., and Wang, N.: Stokes parameter analysis of a packet of turbulence-generating gravity waves, *Journal of Geophysical Research: Atmospheres*, 110, <https://doi.org/10.1029/2004JD005736>, 2005.
- 10 Lyapustin, A., Alexander, M. J., Ott, L., Molod, A., Holben, B., Susskind, J., and Wang, Y.: Observation of mountain lee waves with MODIS NIR column water vapor, *Geophysical Research Letters*, 41, 710–716, <https://doi.org/10.1002/2013GL058770>, 2014.
- Miglietta, M. M., Zecchetto, S., and De Biasio, F.: WRF model and ASAR-retrieved 10 m wind field comparison in a case study over Eastern Mediterranean Sea, *Advances in Science and Research*, 4, 83–88, <https://doi.org/10.5194/asr-4-83-2010>, 2010.
- Miglietta, M. M., Zecchetto, S., and De Biasio, F.: A comparison of WRF model simulations with SAR wind data in two case studies of orographic lee waves over the Eastern Mediterranean Sea, *Atmospheric research*, 120, 127–146, <https://doi.org/10.1016/j.atmosres.2012.08.009>, 2013.
- 15 Miglietta, M. M., Huld, T., and Monforti-Ferrario, F.: Local complementarity of wind and solar energy resources over Europe: an assessment study from a meteorological perspective, *Journal of Applied Meteorology and Climatology*, 56, 217–234, <http://dx.doi.org/10.1175/JAMC-D-16-0031.1>, 2017.
- 20 Mlawer, E. J., Taubman, S. J., Brown, P. D., Iacono, M. J., and Clough, S. A.: Radiative transfer for inhomogeneous atmospheres: RRTM, a validated correlated-k model for the longwave, *Journal of Geophysical Research: Atmospheres*, 102, 16 663–16 682, <https://doi.org/10.1029/97JD00237>, 1997.
- Nappo, C. J.: *An introduction to atmospheric gravity waves*, Academic press, 2 edn., 2013.
- Niu, G.-Y., Yang, Z.-L., Mitchell, K. E., Chen, F., Ek, M. B., Barlage, M., Kumar, A., Manning, K., Niyogi, D., Rosero, E., Tewari, M., and Xia, Y.: The community Noah land surface model with multiparameterization options (Noah-MP): 1. Model description and evaluation with local-scale measurements, *Journal of Geophysical Research: Atmospheres*, 116, <https://doi.org/10.1029/2010JD015139>, 2011.
- 25 Papandrea, E., Casadio, S., Castelli, E., Dinelli, B. M., De Grandis, E., and Bojkov, B.: Validation of the Advanced Infra-Red Water Vapour Estimator (AIRWAVE) Total Column Water Vapour using Satellite and Radiosonde products., *Annals of Geophysics*, 61, <https://doi.org/10.4401/ag-7524>, 2018.
- 30 Sadowsky, J.: Investigation of signal characteristics using the continuous wavelet transform, *Johns Hopkins APL Technical Digest*, 17, 258–269, 1996.
- Salomonson, V. V., Barnes, W., Xiong, J., Kempler, S., and Masuoka, E.: An overview of the Earth Observing System MODIS instrument and associated data systems performance, in: *IEEE International Geoscience and Remote Sensing Symposium*, vol. 2, pp. 1174–1176, IEEE, <https://doi.org/10.1109/IGARSS.2002.1025812>, 2002.
- 35 Schröder, M., Lockhoff, M., Fell, F., Forsythe, J., Trent, T., Bennartz, R., Borbas, E., Bosilovich, M. G., Castelli, E., Hersbach, H., Kachi, M., Kobayashi, S., Kursinski, E. R., Loyola, D., Mears, C., Preusker, R., Rossow, W. B., and Saha, S.: The GEWEX Water Vapor Assessment archive of water vapour products from satellite observations and reanalyses, *Earth System Science Data*, 10, 1093–1117, <https://doi.org/10.5194/essd-10-1093-2018>, 2018.



- Thompson, G., Field, P. R., Rasmussen, R. M., and Hall, W. D.: Explicit forecasts of winter precipitation using an improved bulk microphysics scheme. Part II: Implementation of a new snow parameterization, *Monthly Weather Review*, 136, 5095–5115, <https://doi.org/10.1175/2008MWR2387.1>, 2008.
- Torrence, C. and Compo, G. P.: A practical guide to wavelet analysis, *Bulletin of the American Meteorological society*, 79, 61–78, [https://doi.org/10.1175/1520-0477\(1998\)079<0061:APGTWA>2.0.CO;2](https://doi.org/10.1175/1520-0477(1998)079<0061:APGTWA>2.0.CO;2), 1998.
- Uhlenbrock, N. L., Bedka, K. M., Feltz, W. F., and Ackerman, S. A.: Mountain wave signatures in MODIS 6.7- μ m imagery and their relation to pilot reports of turbulence, *Weather and forecasting*, 22, 662–670, <https://doi.org/10.1175/WAF1007.1>, 2007.
- Vagenas, C., Anagnostopoulou, C., and Tolika, K.: Climatic study of the marine surface wind field over the Greek seas with the use of a high resolution RCM focusing on extreme winds, *Climate*, 5, 29, <https://doi.org/10.3390/cli5020029>, 2017.
- 10 Vosper, S. B., Sheridan, P. F., and Brown, A. R.: Flow separation and rotor formation beneath two-dimensional trapped lee waves, *Quarterly Journal of the Royal Meteorological Society*, 132, 2415–2438, <https://doi.org/10.1256/qj.05.174>, 2006.
- Wang, W., Bruyère, C., Duda, M., Dudhia, J., Gill, D., Lin, H.-C., Michalakes, J., Rizvi, S., and Zhang, X.: ARW version 3 modelling system user's guide, NCAR, Boulder, Colorado, 312 pp., 2010.
- 15 Wurtele, M. G., Datta, A., and Sharman, R. D.: Lee waves: Benign and malignant, NASA-CR-186024, Los Angeles, CA 90024-1565, 26 pp., http://www.nasa.gov/centers/dryden/pdf/88288main_H-1890.pdf, 1993.

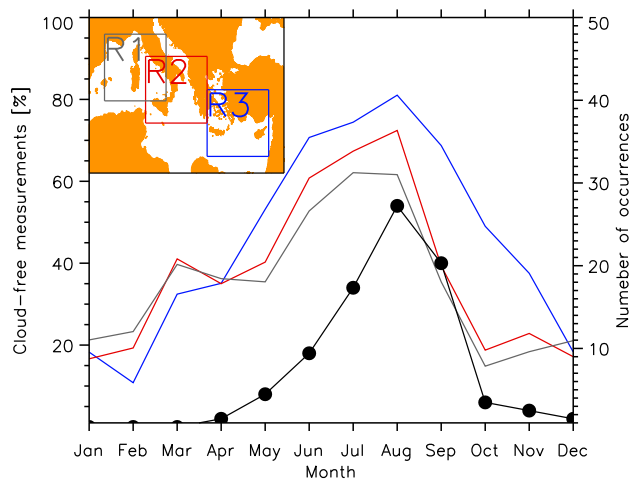


Figure 1. Monthly means of the percentage of cloud-free measurements for the three corresponding areas (shown on the top-left map, R1=grey, R2=red, R3=blue) for year 2003. The total number of lee waves occurrences (ATSR-2 + AATSR for the whole missions) is also reported as a function of the month (black curve, with the scale on the right hand side).

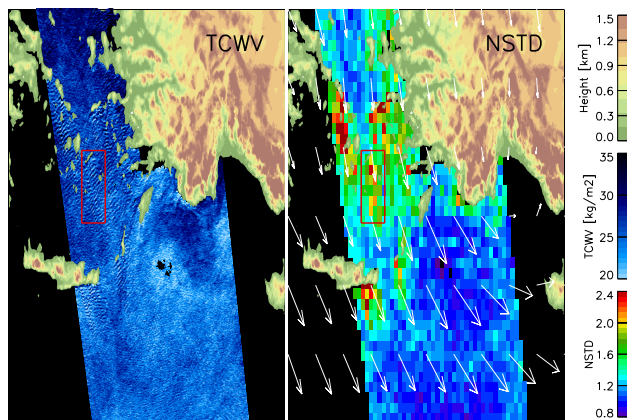


Figure 2. Left panel: AIRWAVE TCWV for 2 Aug 2002, AATSR orbit 2214, ascending. Right panel: corresponding normalised standard deviation. The arrows represent the wind speeds (length) and directions, as derived from ERA-Interim products at $1.0^\circ \times 1.0^\circ$. The bounding box area is studied more in detail in Fig. 4.

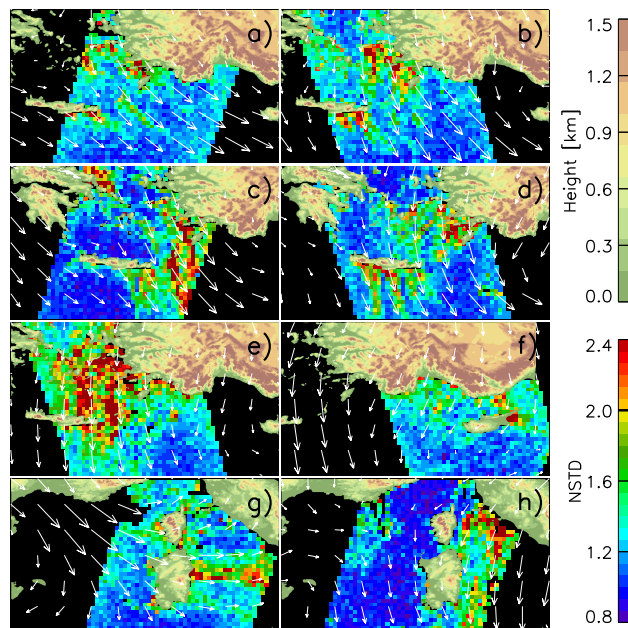


Figure 3. Normalised standard deviation for: a) 23 Jul 1997, ATSR-2 orbit 11798, descending; b) 23 Jul 1997, ATSR-2 orbit 11805, ascending; c) 23 Jul 2002, ATSR-2 orbit 37936, descending; d) 26 Apr 2003, AATSR orbit 6036, ascending; e) 15 Jul 2009, AATSR orbit 38558, ascending; f) 19 Jun 2002, ATSR-2 orbit 37456, ascending; g) 2 Aug 2006, AATSR orbit 23121, descending; h) 27 Jul 2002, ATSR-2 orbit 37994, descending. The arrows represent the wind speeds (length) and directions, as derived from ERA-Interim products at $1.0^{\circ} \times 1.0^{\circ}$.

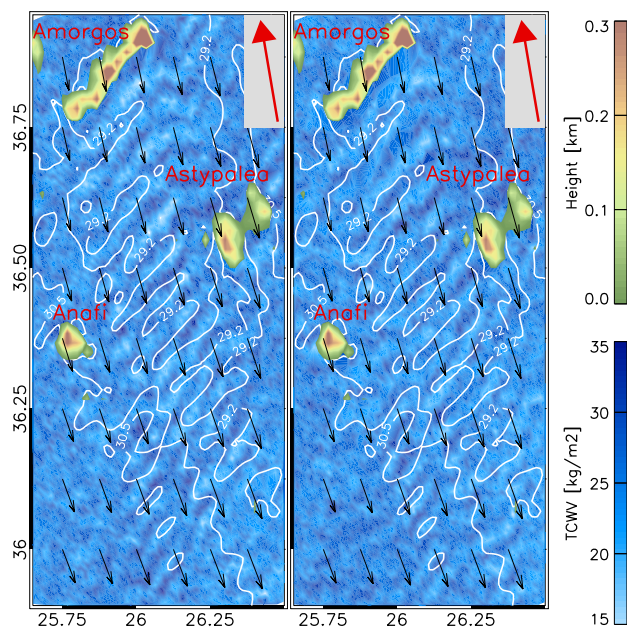


Figure 4. AIRWAVE TCWV (bluish colors) for 2 August 2002 over Aegean Sea derived from: ATSR-2, orbit 38086 (ascending), measurements acquired from 20:11:41 to 20:12:00 (left), AATSR, orbit 2214 (ascending), measurements acquired from 19:43:11 to 19:43:30 (right). The black arrows represent wind speeds (length) and directions, as derived from ERA-Interim fields interpolated at $0.125^\circ \times 0.125^\circ$. Superimposed (white contour lines for two specific values of 29.2 and 30.5 kg m^{-2}), TCWV as computed from WRF model run (output at 20:00:00). The top-right box shows the satellite flying direction.

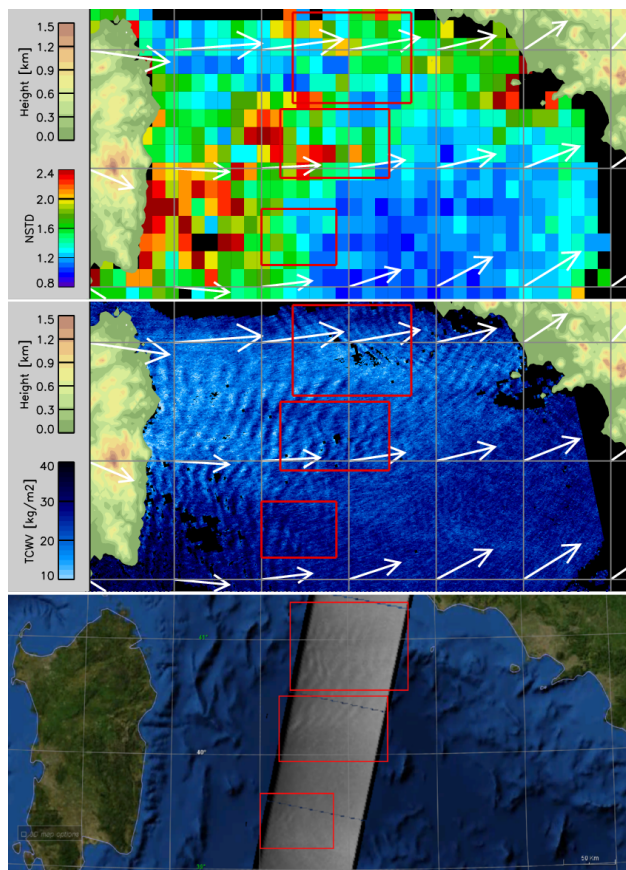


Figure 5. 18 July 1997 over Tyrrhenian Sea. Top panel: NSTD derived from the AIRWAVE TCWV fields (shown in the central panel), ATSR-2, orbit 11734, ascending. The arrows represent the wind speeds (length) and directions, as derived from ERA-Interim fields at $1.0^\circ \times 1.0^\circ$. Bottom panel: SAR/ERS-2 single look complex images, track 351, frames 2763, 2781, 2799, 2817, orbit 11728, descending.

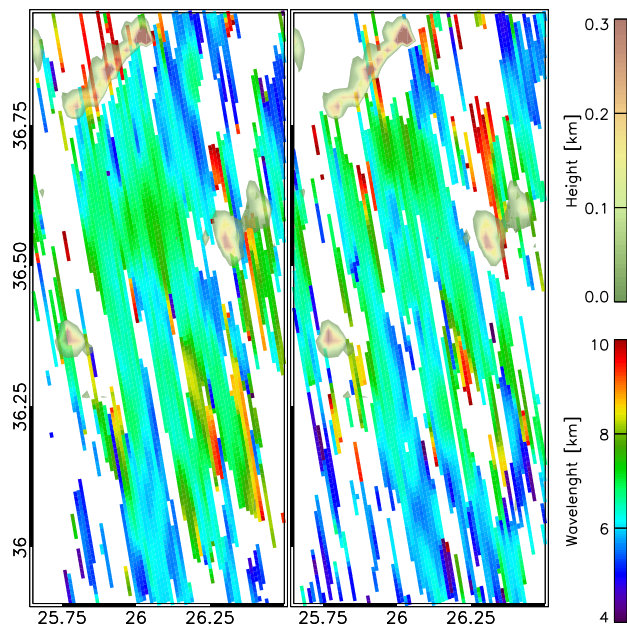


Figure 6. Wavelength, indicated by the lower bar with a colour scale ranging from 4 to 10 km, as derived applying the CWT method over the AIRWAVE TCWV products shown in Fig 4. The left panel shows ATSR-2 orbit 38086 (ascending), the right panel AATSR orbit 2214 (ascending). The height of the ground is also shown (upper bar).